Letter

Few-mode to mesoscopic junctions in gatemon qubits

Alisa Danilenko,[1,*] Deividas Sabonis,[1,*] Georg W. Winkler,[2] Oscar Erlandsson,[1] Peter Krogstrup,[1,3] and Charles M. Marcus[1]

[1]*Center for Quantum Devices, Niels Bohr Institute, University of Copenhagen, 2100 Copenhagen, Denmark*
[2]*Microsoft Quantum, Microsoft Station Q, University of California, Santa Barbara, California 93106-6105, USA*
[3]*Microsoft Quantum Materials Lab–Copenhagen, 2800 Lyngby, Denmark*

(Received 8 September 2022; revised 20 March 2023; accepted 9 May 2023; published 17 July 2023)

We investigate a semiconductor nanowire-based gatemon qubit with epitaxial Al on two facets of the nanowire, allowing gate control of wire density. Two segments have the Al removed, one forming a Josephson junction, and the other operating as a transistor, providing *in situ* switching between dc transport and qubit operation. Gating the nanowire (NW) changes the rate of decay of qubit frequency in magnetic field applied parallel to the NW. Gating the Josephson junction can lead additionally to nonmonotonic behavior of the qubit frequency in parallel magnetic field. A detailed model of the wire and junction yields behavior consistent with experiment, and allows us to propose that gating the bulk wire affects the rate of frequency decay in fields due to changes in the bulk potential distribution, while nonmonotonic behavior of the frequency is due to the interference of Andreev bound states in the junction. Gating the junction further allows access to the multimode regime, where fluctuations in qubit frequency are measured to be considerably smaller than the theoretical "universal" value, also smaller than numerics, and consistent with previous measurements of fluctuating critical currents.

DOI: 10.1103/PhysRevB.108.L020505

Recent materials advances [1] have led to a new approach to Josephson qubit technology based on hybrid superconductor-semiconductor nanowires (NWs) [2,3] and comparable two-dimensional platforms [4]. This approach allows voltage control of qubit operation and reduced sensitivity to charge noise [5–7]. Hybrid NWs can also form the basis of Andreev qubits [8–11], protected $0-\pi$ qubits [12], systems to investigate the presence of topological phases [13], and voltage-controlled qubit couplers [14]. Because the electron wavelength in the semiconductor is comparable to the NW diameter, electronic states under the proximitizing superconductor typically occupy a small number of transverse modes [15]. For NWs with facets not covered by the superconductor, this mode structure can be altered by electrostatic gating [16].

In this Letter, we compare the magnetic field and gate-voltage dependence of gatemon qubits fabricated from epitaxial InAs/Al NWs to a detailed numerical model of the wire and Andreev bound states (ABSs) in the junction [17]. To gather parameters for the model, we take advantage of another feature of hybrid NWs by creating a local field-effect transistor (FET) that allows *in situ* switching between dc transport and circuit quantum electrodynamics (cQED) configurations [5]. Magnetic field and gate-voltage dependencies of qubit frequency f_Q [18] are in reasonable agreement with the model, and consistent with gate-voltage [19] and magnetic field dependencies [20] of critical currents in NW junctions, here measurable in the same qubit junction.

At gate voltages corresponding to several ABSs in the qubit junction, mesoscopic (random, repeatable) fluctuations of qubit frequency as a function of gate voltage were observed. Comparing experimental results with both numerics and theoretical universal statistics for mesoscopic critical current fluctuations [21], we find that the observed qubit-frequency fluctuations, $\sigma_{f_Q} \sim 130$ MHz, corresponding to critical-current fluctuations $\sigma_{I_c} \sim 1$ nA, are smaller than theoretical values for a short junction [21], though consistent with previous experimental values of critical-current fluctuations [22]. We tentatively ascribed the reduced fluctuation of f_Q to nonideal material interfaces [22,23] or a Fermi velocity mismatch between the Al-covered region and the bare semiconductor junction [24] leading to normal reflection competing with Andreev reflection within the junction interfaces.

Devices were fabricated on a high-resistivity silicon substrate covered with a 20-nm NbTiN film, deposited by sputtering. Each chip contains three gatemons based on NWs, about 100 nm in diameter, with two or three of six facets covered with ∼30-nm-thick Al [18], two with FET-switched dc transport capabilities, each with individual resonator readout circuits. Overall, three devices were measured. Data from two devices, yielding consistent results, are reported here. Resonators, transmission line, and electrostatic gates were fabricated using additional layers of sputtered NbTiN, patterned using electron beam lithography and reactive ion etching. Before placing the NW on the bottom gates, a lithographically patterned layer of HfO_2 dielectric was deposited by atomic layer deposition. A micrograph of one of the FET-switched devices is shown in Fig. 1(a). The right side of the NW connects to the ground plane, the left side to a dc contact through the FET, and the center to the qubit island. The Josephson junction, seen inside the white box in Fig. 1(a), is formed by wet etching ∼100 nm of the Al shell. While the

[*]These authors contributed equally to this work.

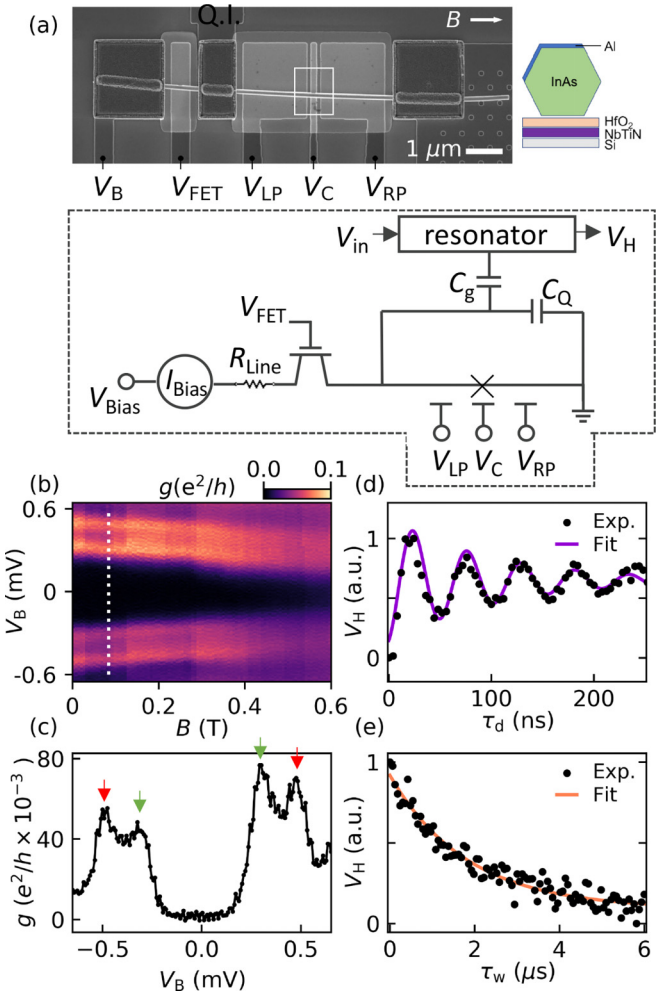

FIG. 1. (a) Scanning electron micrograph of Device 1 (cross-section sketch on the right, device schematic below). The NW is contacted on the right to the ground plane, and the qubit island is connected in the center (labeled Q.I.). The purpose of gate voltage V_C is to control the Josephson junction, while V_{LP} and V_{RP} are intended to tune the bulk wire. Direction of applied magnetic field B is shown. (b) Differential conductance $g \equiv \frac{dI_B}{dV_B}$ as a function of V_B shows the superconducting gap of the junction in applied field, with a cut (c) taken at $B = 0.08$ T. $V_{FET} = +6$ V, $V_{LP} = V_{RP} = 0$ V, $V_C = -3.6$ V. Arrows indicate where Al coherence peaks in the two leads align (red) and where the Al coherence peak in one lead aligns with the subgap ABS in the other lead (green). (d) Rabi oscillations at $B = 0$. Demodulated transmission V_H measured as a function of drive duration τ_d at the qubit frequency $f_Q = 4.37$ GHz. Exponentially decaying sinusoidal fit yields Rabi time $T_2^R = 119$ ns. (e) Qubit relaxation: V_H measured as a function of wait time τ_w between drive and readout pulses. The qubit is excited with a π pulse calibrated from (d). Exponential fit yields $T_1 = 1.8$ μs.

orientation of the shell is not discernible during manual NW placement, scanning electron micrographs taken afterwards can resolve the Al shell. Devices with the shell on the up-facing half of the NW, which allow control of carrier density in the NW by bottom gates, are then measured. Gate voltage V_C, underneath the junction, was used to tune f_Q, while voltages V_{LP} and V_{RP} were used to tune the density in the bulk NW. All measurements were performed in a dilution refrigerator with a base temperature of 20 mK using a 6-1-1 T vector magnet.

Setting the FET in the conducting state by applying +6.0 V on the FET gate, differential conductance $g \equiv dI_B/dV_B$ of the junction was measured as a function of voltage bias V_B. With the qubit junction in the tunneling regime, g can be used to measure the parent gap and ABS features in the semiconductor, as shown in Figs. 1(b) and 1(c). The two higher-bias peaks, marked with red arrows in Fig. 1(c), occur symmetrically around $V_B = 0$ at the bias where coherence peaks from the Al gap, $\Delta \sim 250$ μeV, on the two sides of the junctions align, $V_B \sim \pm 2\Delta/e \sim \pm 0.5$ mV. Since the leads either side of the junction consist of proximitized InAs, the leads themselves can host ABSs. The two lower-bias peaks, marked with green arrows in Fig. 1(c), indicate where the coherence peak in one lead aligns with a subgap ABS in the other lead. Extrapolating the field dependence of the gap gives a field of ∼1.4 T where the gap closes. Following dc transport characterization of the junction, the FET was switched to a nonconductive state (FET gate at −6 V) allowing the device to be operated in cQED mode as a qubit. Setting $V_C = -1.7$ V, $V_{LP,RP} = 0$ V gives a qubit frequency $f_Q = 4.37$ GHz, measured via two-tone spectroscopy. This corresponds to a critical current of ∼10 nA. Rabi oscillations [Fig. 1(d)] were measured by applying a series of pulses of duration τ_d at f_Q and plotting the demodulated transmission V_H as a function of τ_d. Fitting to an exponentially decaying sinusoid yields a Rabi time of 119 ± 1 ns. Qubit relaxation [Fig. 1(e)] was measured by applying a π pulse, found using data in (d), at f_Q, then waiting τ_w before applying a readout pulse at the resonator frequency, 5.46 GHz, giving a V_H signal that decreases with increasing τ_w. An exponential fit yields a qubit lifetime of 1.81 ± 0.13 μs.

The dependence of f_Q on axial magnetic field B and gate voltage is shown in Fig. 2(a), for Device 2, which is similar to Device 1 in material and fabrication. For each value of $V_{LP,RP}$, V_C was compensated to keep the zero-field frequency constant. This adjustment aimed to compensate for the cross-coupling effect of $V_{LP,RP}$ on the junction, since the aim was to tune the bulk wire density, and leave the junction as unaffected as possible. The adjustment was made by sweeping V_C slowly after changing $V_{LP,RP}$ to the new desired value, until the qubit frequency reached the same zero-field value as during the previous data point measurement, indicating that the junction was returned to a similar state as in the previous measurement. This compensation had the added benefit of making sure that f_Q stayed in a measurable range at zero field. The changes made to V_C are very small compared to its full range of operation, and the exact values of V_C for each data point can be found in the Supplemental Material, Fig. S7 [25]. In the measured field and frequency range, the qubit frequency decreased monotonically with increasing B. The solid lines in Fig. 2(a) are simple fits relating the qubit frequency expected closing of the superconducting gap in field, $f_Q(B) = f_Q(0)[1 - (B/B_c)^2]^{1/4}$, where B_c is the critical field [26]. As illustrated in Fig. 2(b), a trend in the dependence on $V_{LP,RP}$ was observed: the more positive the gate voltage applied to the NW, the more rapidly f_Q decayed in the field.

To understand the effect of the gate-voltage configuration on the magnetic field dependence of qubit frequency,

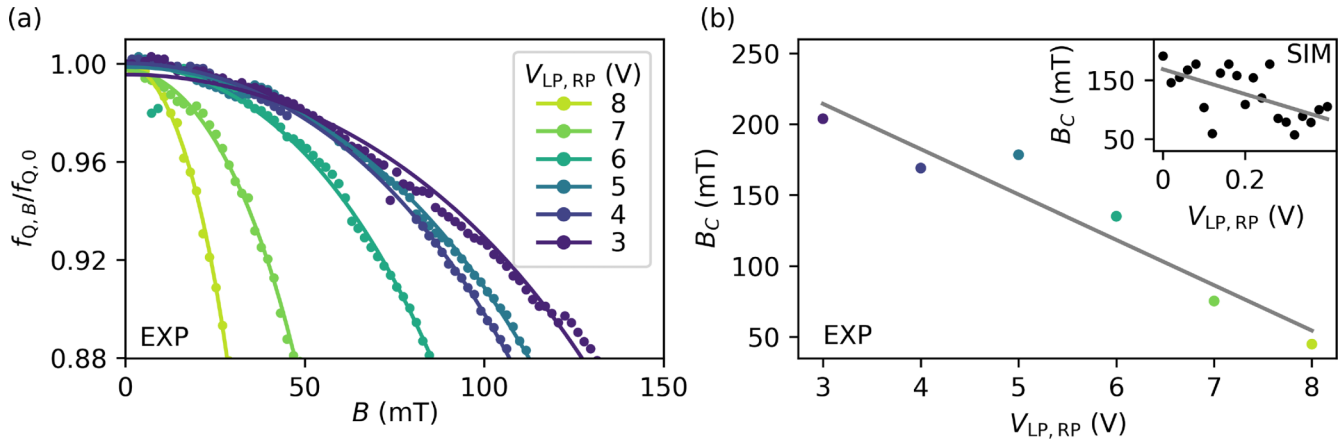

FIG. 2. (a) Measured qubit frequency (normalized) as a function of parallel magnetic field B at a range of $V_{LP,RP}$ values. V_C was compensated to keep the zero-field frequency constant for all gate configurations. (b) Critical field B_c, extracted from fitting the data for each gate configuration measured. Shown with a linear fit.

we perform numerical modeling of the energy spectrum and qubit frequency using codes similar to Refs. [27–29] using a self-consistent Thomas-Fermi approximation, including Zeeman and orbital effects of the magnetic field, treating coupling of the superconductor to the semiconductor in terms of a self-energy boundary condition (see Supplemental Material [25]). We find that the simulated qubit frequency follows roughly the quadratic decay of the parent gap for small fields, as observed in the experiment. The inset in Fig. 2(b) shows the simulated dependence of B_c on the NW gate voltage. It should be noted that the lever arm (defined as the conversion ratio of the gate voltage to the shift in the energy levels) in the simulation is much larger than in experiment, hence the significant difference in absolute gate-voltage values. There is still a trend towards more rapidly decaying f_Q at more positive gate voltage in the simulation, but the numerical results are less monotonic than what we observe in the experiment. The straight line through the data points is a linear fit, and is intended to highlight the overall trend of the data, rather than to imply any mathematical relation. At more negative gate voltages, the wave function is pressed up away from the gates and close to the superconducting shell, reducing the wave function cross section threaded by magnetic flux, leading to a more gradual decay of f_Q in field. Within this interpretation, the effect is due to gating of the NW, not the junction.

With increasing magnetic field, nonmonotonic evolution of f_Q was observed both in experiment and in simulation, as shown in Fig. 3. For the simulation, the corresponding electrostatics of the wire and junction, as well as the field dependence of ABSs in the junction, are shown in Figs. 3(b) and 3(c). The simulated gate configuration here is $V_{LP} = V_{RP} = 0$ V, and $V_C = +0.55$ V. We choose to showcase the simulation for this gate configuration because it was one of the configurations which yielded a nonmonotonic spectrum. While it is not possible to go from our experimentally measured qubit spectrum to a precise Andreev spectrum, by using the simulation we can select the parameters which lead to a similar qubit spectrum, and then compare to the corresponding simulated Andreev spectrum to gain more information. It should be noted that this particular configuration is chosen for illustrative purposes, as one of the nonmonotonic configurations. The full range of simulated qubit spectra can be found in the Supplemental Material. From the simulated electrostatic potential diagram shown in Fig. 3(b), it can be seen that in this configuration the junction gate V_C accumulates electrons, opening the junction, while the back gates $V_{LP,RP}$ are used to deplete, pushing the electron density in the leads towards the superconductor.

The spectrum in Fig. 3(c) shows several ABSs in the junction, a few of which show an oscillatory behavior in field. Since the magnetic field is applied parallel to the NW, flux is threaded through the cross section of the NW. The magnetic field where they have their minimum corresponds roughly to half a magnetic flux quantum through the cross section of the NW.

The energies and phase dependence of ABSs are directly linked to the qubit frequency. To understand the effect of ABS energies on the qubit frequency, we perform numerical modeling of the energy spectrum and qubit frequency using codes similar to Refs. [5,29,30] using a self-consistent Thomas-Fermi approximation, including Zeeman and orbital effects of the magnetic field, treating coupling of the superconductor to the semiconductor in terms of a self-energy boundary condition (see Supplemental Material [25]). The supercurrent is simulated using the KWANT package [31] and the analysis is developed in Refs. [19,32]. The simulated critical current I_c, yields a qubit frequency $f_Q \approx \sqrt{8E_J E_C}/h = \sqrt{2E_C I_c/h\pi e}$ (valid for $E_J \gg E_C$; in the experiment $E_J/E_C \sim 10$), where $E_C = 2$ μeV is estimated from electrostatic simulations of the qubit island [33] and $E_J = \hbar I_c/2e$.

In the simulated qubit frequency as a function of magnetic field [Fig. 3(d)], one can see a lobelike structure where the qubit frequency oscillates as a function of magnetic field. Comparing the simulated ABS spectrum to the simulated behavior of the frequency in field, one can see that the oscillation period of the ABS spectrum is lined up with the qubit frequency—the ABSs reach an energy minimum at the field value where the frequency oscillation occurs, ∼0.125 T. Therefore, we conclude that the oscillatory behavior of the qubit frequency in field is linked to flux modulation of ABSs which form in the junction. Based on these simulations, we

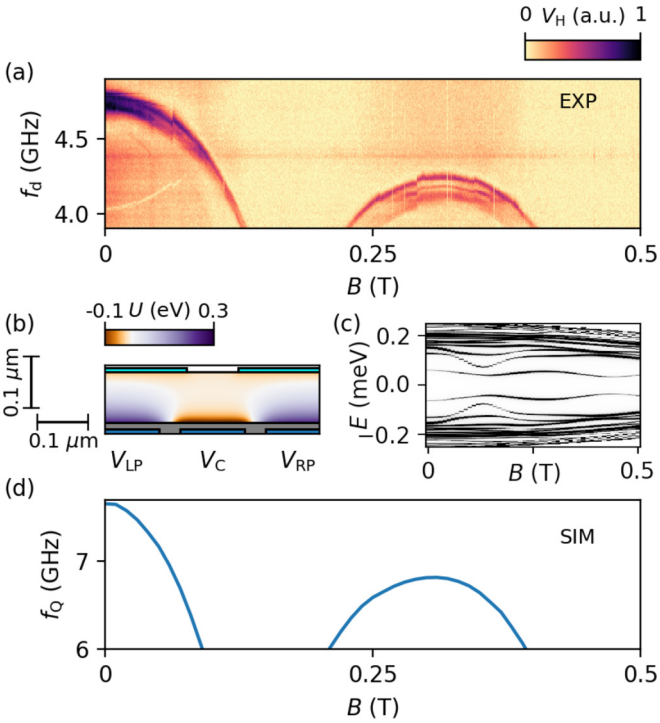

FIG. 3. Two-tone spectroscopy as a function of drive frequency, f_d, and parallel magnetic field, B, with $V_{FET} = +6.0$ V, $V_{LP,RP} = 0$ V, and $V_C = -1.8$ V. At low field, the qubit frequency, f_Q, decreases rapidly, disappearing from the measurement window at $B \sim 130$ mT. At higher field, f_Q recovers, reentering the measurement window at $B \sim 220$ mT, then decreases, leaving the measurement window at $B \sim 400$ mT. (b) Numerical electrostatic potential, U, near the junction on a vertical cut through the NW, for a configuration with nonmonotonic f_Q. The superconductor (Al) is indicated on the top (cyan); due to the positive band offset of 50 meV there is an accumulation layer towards it. The left plunger, the cutter, and the right plunger gates are indicated on the bottom (dark blue). Both plungers are set to the same voltage $V_{LP} = V_{RP} = 0$ V, $V_C = +0.55$ V. (c) Simulated local density of states in the junction region for this gate configuration as a function of parallel magnetic field. A few low-energy ABSs showing flux-modulated oscillations can be found inside the junction. (d) Simulated qubit frequency for the same gate configuration. The flux modulation of ABS results in an oscillation of the qubit frequency.

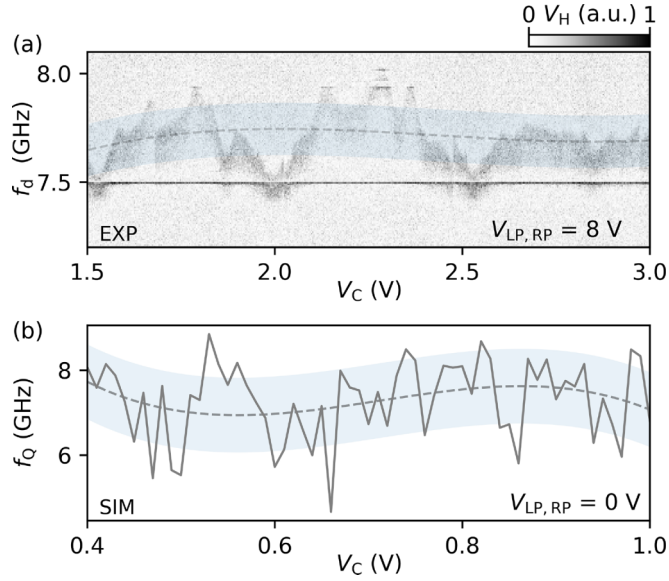

FIG. 4. (a) Two-tone spectroscopy as a function of drive frequency (f_d) and gate voltage V_C. The qubit frequency exhibits mesoscopic fluctuations. The data is fitted with a smoothed spline (dashed line), and the light-blue shading indicates the standard deviation, covering the area within $+/-\sigma$ of the fit. The horizontal resonance at 7.5 GHz is an artifact of the measurement circuit. (b) Simulated trace of qubit frequency. f_Q as a function of gate voltage V_C, with the fluctuations analyzed in a similar manner to the experimental data.

propose that the additional revival observed in the experiment is due to junction-based physics, in contrast to the low-field behavior of f_Q in Fig. 2, which we attribute to depletion within the wire.

Increasing the number of modes in the semiconductor as much as possible by setting gate voltages V_{PL} and V_{PR} to +8 V results in random-looking but repeatable mesoscopic fluctuations of f_Q with V_C. In this regime, E_J/E_C is closer to ∼30. The frequency fluctuates around ∼7.6 GHz, corresponding to a critical current of ∼30 nA. These fluctuations are closely related to mesoscopic fluctuations of critical current in Josephson junctions [21,22,34]. In superconductor–normal–superconductor Josephson junctions with a distance L between superconductors which is long compared to the mean free path, l, in the N region and the superconducting coherence length, ξ, mesoscopic fluctuations of critical current I_c are expected to have a nonuniversal magnitude, with standard deviation $\sigma_{I_c} \sim ev_F l/L^2$, where v_F is the Fermi energy in the N region [35]. On the other hand, in short, disordered junctions $l \ll L < \xi$, critical current fluctuations are expected to be "universal," $\sigma_{I_c} \sim e\Delta_0/\hbar$, independent of junction parameters [21]. Our junction length is ∼100 nm, which we can expect to be in the short junction limit, consistent with previous work [36,37].

Fluctuation statistics were extracted from experimental data by sampling over V_C in Device 2. Figure 4(a) shows two-tone spectroscopy data as a function of junction gate V_C at $B = 0$. We perform these measurements at much more positive gate voltages than in the previous section, such that the number of modes in the junction is maximized. The qubit frequency fluctuation is quantified by fitting a smoothed spline to the trace and extracting a standard deviation, yielding $\sigma_{f_Q} \sim 130$ MHz. This corresponds to critical current fluctuation $\sigma_{I_c} \sim (\pi ehf_Q/E_C)\sigma_{f_Q} \sim 1.0$ nA. This is much smaller than the theoretically predicted value [21] for a short junction, which would give of order ∼50 nA, but is in closer agreement with experiments measuring critical-current oscillations [22,34] which find fluctuations on the order of 1 nA.

Similar traces are simulated for a range of gate voltages, as shown in Fig. 4(b) for simulated $V_{LP,RP} = 0$. Changing the plunger gate voltages can be viewed as a variation in the simulated properties of the junction, which was not attempted in our experiment. The simulated fluctuations in f_Q are in the range 0.4–1 GHz, corresponding to critical-current

fluctuations in the range 3–9 nA. These values are larger than what was observed experimentally, but smaller than the universal value for a short junction.

In conclusion, we have investigated semiconductor-based transmon qubits that allow both dc transport and cQED operation, controlled by a field-effect transistor, and are magnetic field compatible. With the help of numerics, we observe that the rate of qubit frequency decay in field is controllable by gating of the bulk NW, while additional oscillatory behavior at higher fields may be attributed to flux modulation of ABSs in the junction. In the many-channel regime, mesoscopic fluctuations of the qubit frequency were considerably smaller than expected from universal theory, somewhat smaller than numerics, and comparable to previous corresponding results of fluctuations in critical current.

We thank Ruben Grigoryan, Bernard van Heck, Marina Hesselberg, Karthik Jambunathan, Anders Kringhøj, Thorvald W. Larsen, Robert McNeil, Karolis Parfeniukas, Karl Petersson, Lukas Splitthoff, Agnieszka Telecka, Shivendra Upadhyay, Sachin Yadav, and David van Zanten for help with device fabrication and valuable discussion. Research was supported by the Danish National Research Foundation, Microsoft, a grant (Project No. 43951) from VILLUM FONDEN, and the European Research Council under Grant No. HEMs-DAM 716655.

[1] P. Krogstrup, N. Ziino, W. Chang, S. Albrecht, M. Madsen, E. Johnson, J. Nygård, C. Marcus, and T. Jespersen, Nat. Mater. **14**, 400 (2015).

[2] G. de Lange, B. van Heck, A. Bruno, D. J. van Woerkom, A. Geresdi, S. R. Plissard, E. P. A. M. Bakkers, A. R. Akhmerov, and L. DiCarlo, Phys. Rev. Lett. **115**, 127002 (2015).

[3] T. W. Larsen, K. D. Petersson, F. Kuemmeth, T. S. Jespersen, P. Krogstrup, J. Nygård, and C. M. Marcus, Phys. Rev. Lett. **115**, 127001 (2015).

[4] L. Casparis, M. R. Connolly, M. Kjaergaard, N. J. Pearson, A. Kringhøj, T. W. Larsen, F. Kuemmeth, T. Wang, C. Thomas, S. Gronin, G. C. Gardner, M. J. Manfra, C. M. Marcus, and K. D. Petersson, Nat. Nanotechnol. **13**, 915 (2018).

[5] A. Kringhøj, T. W. Larsen, B. van Heck, D. Sabonis, O. Erlandsson, I. Petkovic, D. I. Pikulin, P. Krogstrup, K. D. Petersson, and C. M. Marcus, Phys. Rev. Lett. **124**, 056801 (2020).

[6] A. Kringhøj, B. van Heck, T. W. Larsen, O. Erlandsson, D. Sabonis, P. Krogstrup, L. Casparis, K. D. Petersson, and C. M. Marcus, Phys. Rev. Lett. **124**, 246803 (2020).

[7] A. Bargerbos, W. Uilhoorn, C.-K. Yang, P. Krogstrup, L. P. Kouwenhoven, G. de Lange, B. van Heck, and A. Kou, Phys. Rev. Lett. **124**, 246802 (2020).

[8] M. Hays, G. de Lange, K. Serniak, D. J. van Woerkom, D. Bouman, P. Krogstrup, J. Nygård, A. Geresdi, and M. H. Devoret, Phys. Rev. Lett. **121**, 047001 (2018).

[9] L. Tosi, C. Metzger, M. F. Goffman, C. Urbina, H. Pothier, S. Park, A. L. Yeyati, J. Nygård, and P. Krogstrup, Phys. Rev. X **9**, 011010 (2019).

[10] M. Hays, V. Fatemi, D. Bouman, J. Cerrillo, S. Diamond, K. Serniak, T. Connolly, P. Krogstrup, J. Nygård, A. L. Yeyati, A. Geresdi, and M. H. Devoret, Science **373**, 430 (2021).

[11] F. J. Matute-Cañadas, C. Metzger, S. Park, L. Tosi, P. Krogstrup, J. Nygård, M. F. Goffman, C. Urbina, H. Pothier, and A. L. Yeyati, Phys. Rev. Lett. **128**, 197702 (2022).

[12] T. W. Larsen, M. E. Gershenson, L. Casparis, A. Kringhøj, N. J. Pearson, R. P. G. McNeil, F. Kuemmeth, P. Krogstrup, K. D. Petersson, and C. M. Marcus, Phys. Rev. Lett. **125**, 056801 (2020).

[13] D. Sabonis, O. Erlandsson, A. Kringhøj, B. van Heck, T. W. Larsen, I. Petkovic, P. Krogstrup, K. D. Petersson, and C. M. Marcus, Phys. Rev. Lett. **125**, 156804 (2020).

[14] L. Casparis, N. J. Pearson, A. Kringhøj, T. W. Larsen, F. Kuemmeth, J. Nygård, P. Krogstrup, K. D. Petersson, and C. M. Marcus, Phys. Rev. B **99**, 085434 (2019).

[15] A. Kringhøj, L. Casparis, M. Hell, T. W. Larsen, F. Kuemmeth, M. Leijnse, K. Flensberg, P. Krogstrup, J. Nygård, K. D. Petersson, and C. M. Marcus, Phys. Rev. B **97**, 060508(R) (2018).

[16] L. J. Splitthoff, A. Bargerbos, L. Grünhaupt, M. Pita-Vidal, J. J. Wesdorp, Y. Liu, A. Kou, C. K. Andersen, and B. van Heck, Phys. Rev. Appl. **18**, 024074 (2022).

[17] G. W. Winkler, A. E. Antipov, B. van Heck, A. A. Soluyanov, L. I. Glazman, M. Wimmer, and R. M. Lutchyn, Phys. Rev. B **99**, 245408 (2019).

[18] A. Kringhøj, T. W. Larsen, O. Erlandsson, W. Uilhoorn, J. G. Kroll, M. Hesselberg, R. P. G. McNeil, P. Krogstrup, L. Casparis, C. M. Marcus, and K. D. Petersson, Phys. Rev. Appl. **15**, 054001 (2021).

[19] K. Zuo, V. Mourik, D. B. Szombati, B. Nijholt, D. J. van Woerkom, A. Geresdi, J. Chen, V. P. Ostroukh, A. R. Akhmerov, S. R. Plissard, D. Car, E. P. A. M. Bakkers, D. I. Pikulin, L. P. Kouwenhoven, and S. M. Frolov, Phys. Rev. Lett. **119**, 187704 (2017).

[20] Ö. Gül, H. Y. Günel, H. Lüth, T. Rieger, T. Wenz, F. Haas, M. Lepsa, G. Panaitov, D. Grützmacher, and T. Schäpers, Nano Lett. **14**, 6269 (2014).

[21] C. W. J. Beenakker, Phys. Rev. Lett. **67**, 3836 (1991).

[22] H. Takayanagi, J. B. Hansen, and J. Nitta, Phys. Rev. Lett. **74**, 166 (1995).

[23] Y.-J. Doh, J. Dam, A. Roest, E. Bakkers, L. Kouwenhoven, and S. Franceschi, Science **309**, 272 (2005).

[24] T. Schäpers, A. Kaluza, K. Neurohr, J. Malindretos, G. Crecelius, A. Hart, H. Hardtdegen, and H. Lüth, Appl. Phys. Lett. **71**, 3575 (1997).

[25] See Supplemental Material at http://link.aps.org/supplemental/10.1103/PhysRevB.108.L020505 for experimental setup details, expanded raw experimental data with details of analysis, and expanded simulation results.

[26] M. Tinkham, *Introduction to Superconductivity* (Courier Corporation, North Chelmsford, MA, 2004).

[27] S. Vaitiekėnas, G. W. Winkler, B. van Heck, T. Karzig, M.-T. Deng, K. Flensberg, L. I. Glazman, C. Nayak, P. Krogstrup, R. M. Lutchyn, and C. M. Marcus, Flux-induced topological

superconductivity in full-shell nanowires, Science **367**, eaav3392 (2020).

[28] A. Kringhøj, G. W. Winkler, T. W. Larsen, D. Sabonis, O. Erlandsson, P. Krogstrup, B. van Heck, K. D. Petersson, and C. M. Marcus, Phys. Rev. Lett. **126**, 047701 (2021).

[29] J. Shen, G. W. Winkler, F. Borsoi, S. Heedt, V. Levajac, J.-Y. Wang, D. van Driel, D. Bouman, S. Gazibegovic, R. L. M. Op Het Veld, D. Car, J. A. Logan, M. Pendharkar, C. J. Palmstrøm, E. P. A. M. Bakkers, L. P. Kouwenhoven, and B. van Heck, Phys. Rev. B **104**, 045422 (2021).

[30] S. Vaitiekėnas, P. Krogstrup, and C. M. Marcus, Phys. Rev. B **101**, 060507(R) (2020).

[31] C. W. Groth, M. Wimmer, A. R. Akhmerov, and X. Waintal, New J. Phys. **16**, 063065 (2014) (the code is publicly available at https://kwant-project.org/).

[32] V. P. Ostroukh, B. Baxevanis, A. R. Akhmerov, and C. W. J. Beenakker, Phys. Rev. B **94**, 094514 (2016).

[33] COMSOL, Inc. (www.comsol.com).

[34] H. Y. Günel, I. Batov, H. Hardtdegen, K. Sladek, A. Winden, K. Weis, G. Panaitov, D. Gruetzmacher, and T. Schaepers, J. Appl. Phys. **112**, 034316 (2012).

[35] B. Altshuler and B. Spivak, Zh. Eksp. Teor. Fiz. **92**, 609 (1987).

[36] D. van Woerkom, A. Proutski, B. Heck, D. Bouman, J. Väyrynen, L. Glazman, P. Krogstrup, J. Nygård, L. Kouwenhoven, and A. Geresdi, Nat. Phys. **13**, 876 (2017).

[37] E. Spanton, M. Deng, S. Vaitiekenas, P. Krogstrup, J. Nygård, C. Marcus, and K. Moler, Nat. Phys. **13**, 1177 (2017).